

## Accepted Article

**Title:** Rapid access to ordered mesoporous carbons for chemical hydrogen storage

**Authors:** Uiseok Jeong, HyeonJi Kim, Sreerangappa Ramesh, Nesibe A. Dogan, Sirinapa Wongwilawan, Sungsu Kang, Jungwon Park, Eun Seon Cho, and Cafer T Yavuz

This manuscript has been accepted after peer review and appears as an Accepted Article online prior to editing, proofing, and formal publication of the final Version of Record (VoR). This work is currently citable by using the Digital Object Identifier (DOI) given below. The VoR will be published online in Early View as soon as possible and may be different to this Accepted Article as a result of editing. Readers should obtain the VoR from the journal website shown below when it is published to ensure accuracy of information. The authors are responsible for the content of this Accepted Article.

**To be cited as:** *Angew. Chem. Int. Ed.* 10.1002/anie.202109215

**Link to VoR:** <https://doi.org/10.1002/anie.202109215>

## RESEARCH ARTICLE

# Rapid access to ordered mesoporous carbons for chemical hydrogen storage

Uiseok Jeong,<sup>[a,h]</sup> HyeonJi Kim,<sup>[a,h]</sup> Sreerangappa Ramesh,<sup>[b]</sup> Nesibe A. Dogan,<sup>[c]</sup> Sirinapa Wongwilawan,<sup>[a]</sup> Sungsu Kang,<sup>[d]</sup> Jungwon Park,<sup>[d,e]</sup> Eun Seon Cho\*<sup>[a]</sup> and Cafer T. Yavuz\*<sup>[a,b,f,g]</sup>

- [a] Dr. U. Jeong, H. Kim, S. Wongwilawan, Prof. E. S. Cho, Prof. C. T. Yavuz  
Department of Chemical and Biomolecular Engineering  
Korea Advanced Institute of Science and Technology (KAIST)  
Daejeon 34141, Republic of Korea  
E-mail: [escho@kaist.ac.kr](mailto:escho@kaist.ac.kr)
- [b] Dr. S. Ramesh, Prof. C. T. Yavuz  
Graduate School of EEWS  
Korea Advanced Institute of Science and Technology (KAIST)  
Daejeon 34141, Republic of Korea  
E-mail: [cafer.yavuz@kaust.edu.sa](mailto:cafer.yavuz@kaust.edu.sa)
- [c] Dr. N. A. Dogan  
Department of Bioproducts and Biosystems  
School of Chemical Engineering  
Aalto University, P.O. Box 16300, 00076 Aalto, Finland
- [d] S. Kang, J. Park  
School of Chemical and Biological Engineering and Institute of Chemical Process  
Seoul National University  
Seoul 08826, Republic of Korea
- [e] J. Park  
Center for Nanoparticle Research  
Institute for Basic Science (IBS)  
Seoul 08826, Republic of Korea
- [f] Prof. C. T. Yavuz  
Advanced Membranes & Porous Materials Center, Physical Science & Engineering (PSE)  
King Abdullah University of Science and Technology (KAUST)  
Thuwal 23955, Saudi Arabia
- [g] Prof. C. T. Yavuz  
KAUST Catalysis Center, Physical Science & Engineering (PSE)  
King Abdullah University of Science and Technology (KAUST)  
Thuwal 23955, Saudi Arabia
- [h] These authors contributed equally.

Supporting information for this article is given via a link at the end of the document.

**Abstract:** Ordered mesoporous carbon materials offer robust network of organized pores for energy storage and catalysis applications, but suffer from time-consuming and intricate preparations hindering their widespread use. Here we report a new and rapid synthetic route for a N-doped ordered mesoporous carbon structure through a preferential heating of iron oxide nanoparticles by microwaves. A nanoporous covalent organic polymer is first formed in situ covering the hard templates of assembled nanoparticles, paving the way for a long-range order in a carbonaceous nanocomposite precursor. Upon removal of the template, a well-defined cubic mesoporous carbon structure was revealed. The ordered mesoporous carbon was used in solid state hydrogen storage as a host scaffold for NaAlH<sub>4</sub>, where remarkable improvement in hydrogen desorption kinetics was observed. The state-of-the-art lowest activation energy of dehydrogenation as single step was attributed to their ordered pore structure and N-doping effect.

## Introduction

Mesoporous carbon structures have been extensively studied due to their potential in adsorption, separation, energy storage, drug delivery, catalysis with ordered and uniform pore channel, high surface area and large pore volume.<sup>[1]</sup> Since the introduction of the highly ordered mesoporous carbon structure (CMK-1) by Ryoo's group<sup>[2]</sup>, various synthetic routes have been developed and reported by using templates<sup>[2-3]</sup> such as soft templating<sup>[4]</sup>, hard templating<sup>[5]</sup>, multiple templating<sup>[6]</sup> and in-situ templating<sup>[7]</sup> methods. In addition, heteroatoms such as boron and nitrogen were incorporated into the pristine mesoporous carbons, for enabling their use in catalysis and electrochemistry. In particular, nitrogen-doped mesoporous carbon materials have attracted much attention owing to their exceptional performances in energy storage<sup>[8]</sup>, sensors<sup>[9]</sup>, and ORR reduction<sup>[5e, 10]</sup> by increasing surface energy and reactivity. Because of the well-ordered pore structure and the tunable functionalities upon incorporation of heteroatoms, ordered mesoporous carbon materials are frequently employed as effective platforms for nanoconfinement in forming functional nanocomposites. For example, metal particles can be nanoconfined within such

## RESEARCH ARTICLE

mesoporous carbons, leading to uniform and ordered hybrid structures with superior performances in energy storage or catalysis. In all such cases, the enhancements are mainly attributed to a controlled nanostructure, long range order, and interaction with doped heteroatoms of the ordered mesoporous carbons. The bottleneck for the widespread use of ordered mesoporous carbons is the lengthy procedures and steps required in conventional synthetic routes<sup>[11]</sup>, such as in evaporation-induced self-assembly.<sup>[4b]</sup> The methods often demand careful, time consuming manufacturing techniques, and prolonged heating to produce the mesoporous templates (Figure S1). A new approach is clearly needed, both in the assembly of hard templates and in heating profiles. In our quest of finding alternative paths, we envisioned that rapid self-assembly of uniform nanoparticles could alleviate the need for controlled assembly. And contrary to their ubiquitous use in organic synthesis<sup>[12]</sup>, we discovered that microwave heating has never been employed in ordering nanoparticle based hard templates for the mesoporous templating procedures. Existing literature mainly employs microwaves to facilitate rapid reaction and pyrolysis.<sup>[13]</sup>

One promising application for ordered mesoporous carbons is to be active hosts for hydrogen storage materials, where solid-state hydrogen storage techniques have become important for efficient and safe use of hydrogen as a future fuel. Among various hydrogen storage media, complex hydrides such as  $\text{NaAlH}_4$  have been considered as leading materials on account of their high volumetric hydrogen storage capacities.<sup>[14]</sup> However, their practical use has been limited because of kinetic and thermodynamic barriers associated with hydrogen sorption. To resolve such drawbacks, complex hydrides have been introduced into porous scaffolds for nanoconfinement, leading to enhanced kinetics and thermodynamic hydrogen sorption characteristics.<sup>[15]</sup> The size of confined complex hydride depends on the pore size of scaffold; thus, it is expected that a nanoconfinement effect on hydrogen sorption property of complex hydride is also determined by the pore structure of hosts. In addition, doping elements such as Ti, Ni, and N within mesoporous materials also play a catalytic role in hydrogen release and uptake of complex hydride due to an interfacial charge transfer and new structure formation.<sup>[16]</sup> In this respect, a controllable structure of mesoporous scaffold is critical to tailor hydrogen storage characteristics of confined complex hydrides.

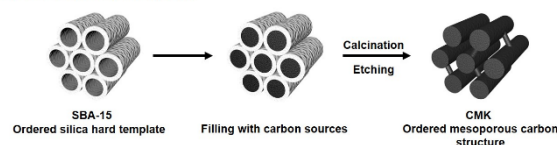
In this work, we report a new and facile synthetic route for nitrogen-doped ordered mesoporous carbons using microwave preferential heating and show their use in effective nanoconfinement of  $\text{NaAlH}_4$  for solid-state hydrogen storage, expecting both nanoscaling and nitrogen doping effects. We employ iron oxide ( $\text{Fe}_3\text{O}_4$ ) nanoparticles as hard templates and self-assemble with polymeric precursors before a rapid microwave heating to form ordered nanocomposites. We call this new approach as 'preferential heating and assembly for nanoparticle templated ordered mesoporous materials' (PHANTOM) method. The ordered mesoporous carbons as a confinement template provide a remarkable change in the dehydrogenation kinetics and associated mechanism of  $\text{NaAlH}_4$

ascribed by the nanoporous structure and doped-nitrogen elements, making a great leap in chemical hydrogen storage.

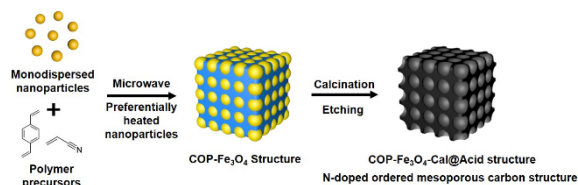
## Results and Discussion

Microwaves provide preferential heating of the hard templates. Towards the goal of rapidly achieving ordered carbons, we first set out to attempt a new strategy to synthesize nitrogen embedded ordered mesoporous carbon structures by microwave irradiation (Scheme 1). By using the porous network framework of a covalent organic polymer (COP) as a rigid organic filler, we synthesized high nitrogen containing, hard templated carbon superstructure. For hard templates, we employed easily synthesized, air stable iron oxide ( $\text{Fe}_3\text{O}_4$ ) nanoparticles. Acrylonitrile (AN) is used as both carbon and nitrogen sources, as well as a linker to arrange nitrogen atoms in the carbon template.

## Conventional method



## PHANTOM method



**Scheme 1.** Microwave heating for preferential assembly. Comparison of a conventional synthetic route with preferential heating and assembly for nanoparticle templated ordered mesoporous materials (PHANTOM) method.

We then prepared covalent organic polymer (COP-122) that is mixed with  $\text{Fe}_3\text{O}_4$  nanoparticles as carbon precursors, but initially, it required more than one day of heating for complete crosslinking. And then almost all of the  $\text{Fe}_3\text{O}_4$  nanoparticles were aggregated and phased out without properly encapsulating on the COP structures (Figure S2). This prompted us to exploit preferential heating through microwaves.

In a first attempt of its kind, COP-122- $\text{Fe}_3\text{O}_4$  nanocomposites were successfully prepared in a dramatically decreased polymerization time (30 min) and with a highly ordered arrangement of  $\text{Fe}_3\text{O}_4$  particles (Figure S3, 4). This confirmed our choice in developing a PHANTOM concept that utilizes hard templates being the primary thermal sources for superior packing mechanisms. In successive control experiments, both neat COP and COP- $\text{SiO}_2$  mixtures failed to make any product under the same microwave irradiation conditions (Table S1). We, therefore, concluded that (1) the porous network needs to be formed in situ, and (2) strong microwave absorbing iron oxide dispersed in non-aqueous media needed to stream-line packing in a biphasic system. Hence, we focused our study on a hexane

## RESEARCH ARTICLE

dispersion of Fe<sub>3</sub>O<sub>4</sub> nanoparticles with COP-122 forming and wrapping the nanoparticle assembly. To obtain an ordered array of hard templates, a monodispersed Fe<sub>3</sub>O<sub>4</sub> solution was prepared (Figure S5, oleic acid coated Fe<sub>3</sub>O<sub>4</sub> nanocrystals dispersed in hexane)<sup>[17]</sup> and mixed with covalent organic polymer precursors (COP-122)<sup>[18]</sup> in a Teflon tube, followed by heating at 90 °C for 30 min in the microwave oven. The hydrophobic Fe<sub>3</sub>O<sub>4</sub> nanoparticles promptly self-assembled on the polyol/water surface without any treatment. As predicted, the microwave irradiation preferentially heated the iron oxide within the assembled clusters because of the significant difference in polarizability of the inorganic nanocrystalline media as opposed to flexible, organic, non-polar polymer linkages. Once complete, the COP-Fe<sub>3</sub>O<sub>4</sub> (CF) powder was calcined at various

temperatures, followed by carbonization under Argon atmosphere, and treated with concentrated acid to remove Fe<sub>3</sub>O<sub>4</sub> particles from the carbon structure. The CF-Calcination-Acid treatment structures (CFC-@XA) exhibited increased surface areas, uniform pore sizes and ordered mesoporous structures. We denoted these new ordered mesoporous carbons as CFC@XA, where 'X' refers to the calcined temperature for pyrolysis of mesoporous carbon structures and 'A' indicates the acid treatment.

Figure 1 shows structural properties of the synthesized nanomaterials. As evident from the TEM images, the uniform Fe<sub>3</sub>O<sub>4</sub> nanoparticles carry their monodispersity to the nanocomposite nanocomposites within the COP framework (Figure 1a, b).

**Table 1.** Comparison table of physical properties of obtained mesoporous carbon structures.

Sample	S <sub>BET</sub> <sup>a</sup> (m <sup>2</sup> g <sup>-1</sup> )	S <sub>mic</sub> <sup>b</sup> (m <sup>2</sup> g <sup>-1</sup> )	V <sub>t</sub> <sup>c</sup> (cm <sup>3</sup> g <sup>-1</sup> )	V <sub>mic</sub> <sup>d</sup> (m <sup>3</sup> g <sup>-1</sup> )	D <sub>p</sub> <sup>e</sup> (nm)	C <sup>f</sup> (wt %)	N <sup>f</sup> (wt %)	O <sup>f</sup> (wt %)	H <sup>f</sup> (wt %)	CO <sub>2</sub> uptake <sup>g</sup> (mmol g <sup>-1</sup> )
CF	32	-	0.1311	-	9.08	48.19	2.05	17.42	4.52	0.48
CFA	53	4	0.1611	0.0030	9.11	82.46	3.22	2.98	7.60	0.81
CFAC@500	344	79	0.1654	0.0220	9.10	88.45	1.60	1.28	3.70	2.12
CFC@500A	478	234	0.6845	0.1052	8.95	74.63	1.60	5.93	3.07	1.90
CFC@600A	244	83	0.5211	0.0379	8.94	86.85	0.80	1.93	1.53	1.71
CFC@700A	199	114	0.6357	0.0461	8.82	88.34	0.38	0.86	1.02	0.95
CFC@800A	289	98	0.4259	0.0476	8.94	88.76	0.24	1.01	0.53	1.24

[a] BET specific surface areas evaluated in p/po from 0.05 to 0.25. [b] Micropore surface areas calculated through the t-plot method. [c] Total pore volumes estimated based on the volume absorbed at p/po of ~ 0.995. [d] Micropore volumes calculated through the t-plot method. [e] pore size derived from the adsorption branches of the isotherms by using the BJH method. [f] Chemical composition data from elemental analysis (C,N,O,H). The left-over inorganic solids constitute the remaining balance of the elemental content. In higher temperature annealed samples, the inorganics tend to sinter and subsequently be etched out more effectively. [g] CO<sub>2</sub> uptake capacity at 273 K and 1.0 bar.

The challenge, however, was to achieve a reproducible calcination and digestion routine that preserve the long-range order. We prepared a series of samples by varying the synthetic conditions. First, the temperature of calcination was set from 500–800 °C. Below 500 °C, the calcination didn't complete. In another series, we digested the embedded iron oxide prior to calcination (CFAC@X). All these samples were subjected to thorough analysis, in particularly the porosity and crystallographic assessments (Figure S6-11, 13-15). We found that if calcination goes over 600 °C, the order fails to hold and aggregation is inevitable. This is because the hard templating Fe<sub>3</sub>O<sub>4</sub> nanoparticles tend to show sintering and Ostwald ripening, leading to polydisperse assemblies devoid of a long-range order. And if acid digestion precedes the calcination, then the pores collapse and give very low porosities with clear lack of uniformity (Figure S12-15). The extensive TEM and SEM imaging on these samples along with TEM-EDX mapping confirmed the observations (Figure S16, 17). The CF sample that was calcined at 500 °C (CFC@500A), however, showed ordered and uniform

mesoporous carbon structure without any deleterious signs from calcination or acid digestion (Figure 1c, d).

The mesoporous properties of CFC@XA structures were investigated with Brunauer-Emmett-Teller (BET) N<sub>2</sub> isotherms and pore size distributions were obtained using both Barrett, Joyner and Halenda (BJH) and nonlocal density functional theory (NLDFT) methods (Figure 1e, f and S18). In particular, the N<sub>2</sub> adsorption-desorption isotherms of CFC@500A demonstrates IUPAC type IV BET curve with a H2 hysteresis loop<sup>[19]</sup>, indicating the uniform microporous and mesoporous structure with bottle type of pore geometries. The BET surface areas, total pore volumes, average pore sizes of all the synthesized structures are summarized in Table 1. The small portion of micropore volume originates from the COP-122 structure, and the large amount of increased total pore volume is ascribed by the uniform mesoporous structure from the ordered Fe<sub>3</sub>O<sub>4</sub> nanoparticle templated voids. Both BET surface area and total pore volume substantially increased for CFC@500A, compared

## RESEARCH ARTICLE

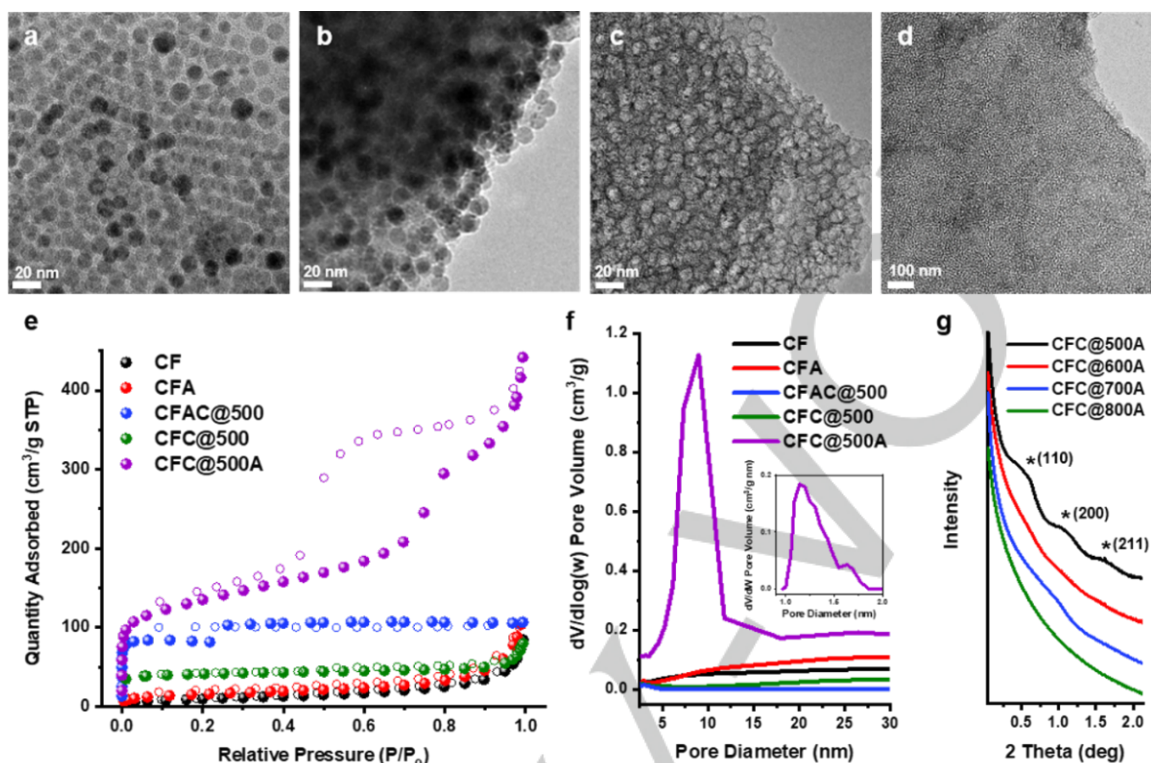


**Figure 1.** Physical properties of COP-Fe<sub>3</sub>O<sub>4</sub> (CF) structures. TEM images of a) monodispersed Fe<sub>3</sub>O<sub>4</sub> nanoparticles in hexane, b) as synthesized CF particles, and c), d) CFC@500A samples. e), f) N<sub>2</sub> adsorption-desorption isotherms (77 K) and the corresponding pore size distribution of synthesized samples. g) SAXRD patterns reflecting long range of mesopores.

to the initial CF structure (32 vs 478 m<sup>2</sup> g<sup>-1</sup> and 0.1311 vs 0.6845 cm<sup>3</sup> g<sup>-1</sup>, respectively). On the other hand, the surface area of CFC@600-800A structures decreased to 244, 199 and 289 m<sup>2</sup> g<sup>-1</sup>, respectively. Furthermore, only CFC@500A presented a strongly concentrated and increased BJH pore size distribution peak at 8.95 nm (Figure 1f and S18).

The transformation of CFC@XA structures during the synthetic process were further examined to understand the chemical nature of the mesoporous materials. The crystalline structure of Fe<sub>3</sub>O<sub>4</sub> particles was converted into pure Fe and Fe<sub>3</sub>C upon calcination at the temperature higher than 600 °C as shown in the X-ray diffraction (XRD) pattern (Figure S19). Furthermore, even after acid treatment these high temperature samples still contained large amount of Fe residue in the carbon structure as a carbide along with graphite, except in the ordered sample CFC@500A. In the small angle X-ray diffraction (SAXRD) measurement (Figure 1g), the CFC@500A shows strong peaks at 0.55°, 1.10° and 1.65°, which correspond to (110), (200), (211) planes, respectively, of the Im $\bar{3}$ m space group, supporting that the obtained ordered mesoporous carbon consists of 3-D cubic crystalline structure.<sup>[20]</sup>

In the Raman spectra of CFC@500 and CFC@500A (Figure S20), two bands are observed clearly at 1345 and 1595 cm<sup>-1</sup>, which explains the C-C single bonds between sp<sup>3</sup> hybridized carbon atoms and in-plane displacement of the sp<sup>2</sup> bonded carbons, respectively. It supports that the carbon structures of CFC@500A sample are well preserved during the

acid treatment. Furthermore, all the prepared samples possess the thermal stability up to 400 °C in air, while the carbons calcined at higher temperatures tend to be more stable, as shown in thermogravimetric analysis (TGA) (Figure S21). The chemical environment and structure of each CFC@XA sample were further investigated by elemental analysis (EA) and X-ray photoelectron spectroscopy (XPS). The EA data show the trend of atomic ratio in the samples depending on the calcined temperature. When the pyrolysis temperature increased from 500 to 800 °C, the content of nitrogen in the structure decreased from 1.6 % to 0.24 % (Table 1). The elevated temperatures clearly foster decomposition through nitric oxides, bringing further disordering in the otherwise ordered mesoporous networks. In the XPS analysis, three distinct nitrogen functional groups associated with carbon, which include pyridinic, pyrrolic, and graphitic nitrogen, were detected, along with nitrate for CFC@500A. (Figure S22).

CO<sub>2</sub> uptake confirms high nitrogen loading. The N-embedded CFC@A mesoporous carbon structures revealed enhanced CO<sub>2</sub> adsorption capacity (Figure S23), a clear evidence for high loading of nitrogen throughout the mesoporous domain. For our main purpose of metal hydride dehydrogenation, it is crucial that we sustain a high heteroatom content to enhance catalysis. In general, CO<sub>2</sub> uptake capacity is dependent on the surface area, heteroatom content, and morphology of the adsorbent. However, in the adsorption results (Table 1), CFAC@500 sample showed highest CO<sub>2</sub> uptake even though

## RESEARCH ARTICLE

the pore sizes shrunk after calcination. This is likely due to the physical property of the transformed and shriveled CFAC@500 which lost its mesoporous property. At the 273 K, CFC@XA structure showed higher CO<sub>2</sub> uptake of 1.90, 1.71, 0.95 and 1.24 mmol g<sup>-1</sup> than original CF structure (0.48 mmol g<sup>-1</sup>, Table 1). CFC@500A showed four times increased CO<sub>2</sub> adsorption capacity than CF. The other CFC@A structures showed decreasing CO<sub>2</sub> uptake along with the lower embedded nitrogen content. Furthermore, we performed gas adsorption and desorption test at 273, 298 and 323 K (CO<sub>2</sub>, N<sub>2</sub>, CH<sub>4</sub>) to check the gas selectivity of CFC@A structures (Figure S23-25). By using the ideal adsorbed solution theory (IAST), CFC@500A (8

- 56) and CFC@600A (44 - 47) demonstrated larger CO<sub>2</sub> / N<sub>2</sub> (15:85) selectivity than others at 1 bar (Figure S26 and Table S2). In order to reveal the surface affinity of the CFC@A structures to CO<sub>2</sub>, the isosteric heat of adsorption (Q<sub>st</sub>) was calculated by using the Clausius-Clapeyron Equation (Figure S27). The Q<sub>st</sub> value at the initial adsorption stage mainly reflects the interaction strength between CO<sub>2</sub> and the adsorbent.<sup>[21]</sup> CFC@500A exhibits higher initial Q<sub>st</sub> value of 32.94 kJ.mol<sup>-1</sup> than the CFC@600, 700, 800A, where Q<sub>st</sub> are 29.27, 11.89 and 25.41 kJ.mol<sup>-1</sup>, respectively.

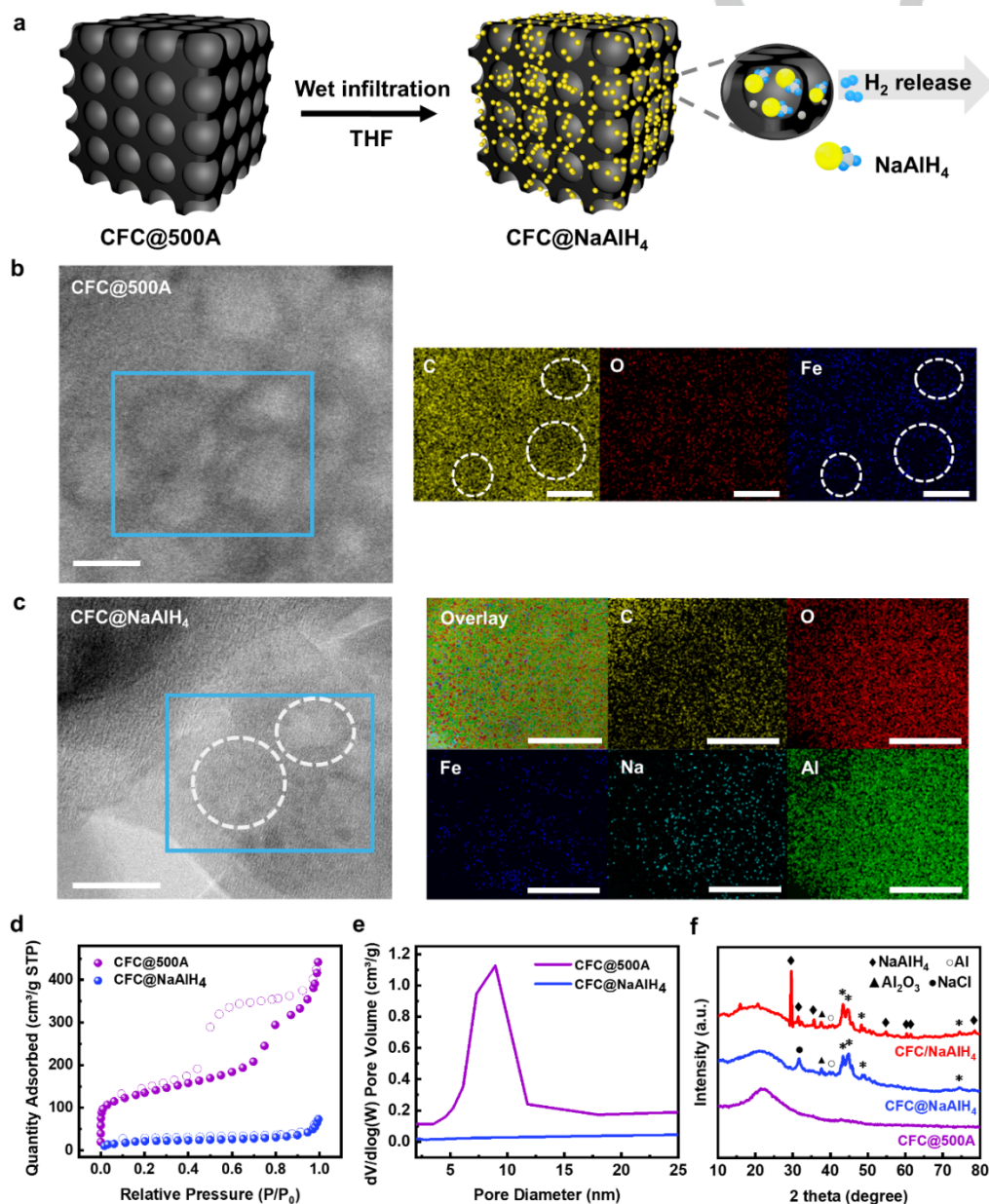


**Figure 2.** Nanoconfinement of NaAlH<sub>4</sub> in CFC@500A. a) Scheme of NaAlH<sub>4</sub> wet infiltration method into CFC@500A (CFC@NaAlH<sub>4</sub>). STEM-EDS images of b) CFC@500A and c) CFC@NaAlH<sub>4</sub> in which the white circles indicate the nanopores of CFC@500A (all scale bars are 10 nm). d) N<sub>2</sub> adsorption-desorption isotherms (77 K) of as-prepared samples and e) the pore size distribution of CFC@NaAlH<sub>4</sub> compared with CFC@500A. f) PXRD patterns of CFC@500A, CFC@NaAlH<sub>4</sub>, and CFC@NaAlH<sub>4</sub> (\*mark represents the peaks from stainless steel sample holder which was used to prevent air exposure of the samples).

## RESEARCH ARTICLE

The CFC@500A is employed as a nanoconfinement host scaffold for NaAlH<sub>4</sub>, expecting both nanoscaling and catalytic effects on hydrogen storage properties from the well-ordered pore structure and uniform N-doping, respectively. A nanocomposite of NaAlH<sub>4</sub> and CFC@500A (CFC@NaAlH<sub>4</sub>) was synthesized to examine the influence of mesoporous carbon scaffolds on hydrogen storage property of confined NaAlH<sub>4</sub>. Also, a simple physical mixture of NaAlH<sub>4</sub> and CFC@500A (CFC/NaAlH<sub>4</sub>) was prepared as a control sample to scrutinize the nanoconfinement effect (further details can be found in the Experimental Procedures). Figure 2a represents a scheme to illustrate that both 1-2 nm and 8-10 nm pores were filled by nanosized NaAlH<sub>4</sub> through wet infiltration using THF as a solvent. The homogeneous pores which have both 1-2 nm and 8-10 nm sizes were formed by chemical bonding within polymer precursors and Fe<sub>3</sub>O<sub>4</sub> nanoparticles, respectively. To demonstrate the incorporated NaAlH<sub>4</sub> within nanopores of carbon scaffold, Bright Field-Scanning Transmission Electron Microscopy-Energy Dispersive X-ray Spectroscopy (BF-STEM-EDS) was implemented for pristine CFC@500A and CFC@NaAlH<sub>4</sub> (Figure 2b, c). According to CFC@500A STEM-EDS, the brighter regions with near-circular shapes represent nanopores where less carbon tends to be detected in EDS mapping, as indicated by white circles (Figure 2b). Also, the residual Fe<sub>3</sub>O<sub>4</sub> particles were identified mainly around the pores, not inside the pores of CFC@500A supported by Fe mapping. Similarly, for CFC@NaAlH<sub>4</sub>, carbon is uniformly distributed and less detected on nanopores specified, and Fe<sub>3</sub>O<sub>4</sub> particles were also found outside the pores as shown in STEM-EDS measurements of CFC@NaAlH<sub>4</sub> (Figure 2c). However, Na and Al were newly detected in identical regions, while the intensity of Na mapping was lower than Al due to electron beam damage of Na.<sup>[22]</sup> Al<sub>x</sub>O<sub>y</sub> was likely formed by air exposure during the specimen transfer process to the TEM. Notably, Na was identified where carbon mapping showed weak intensity which implies nanopores, demonstrating the presence of infiltrated NaAlH<sub>4</sub> into CFC@500A pores. The surface area of CFC@NaAlH<sub>4</sub> significantly decreases, compared to that of the neat CFC@500A, of which values are 478 m<sup>2</sup> g<sup>-1</sup> and 80 m<sup>2</sup> g<sup>-1</sup>, respectively, from BET isotherms (Figure 2d, e). Also, no significant pore volume was identified, as opposed to the carbon template, CFC@500A, in which case it was measured as 0.6845 cm<sup>3</sup> g<sup>-1</sup> (Table 1). This result indicates that NaAlH<sub>4</sub> was confined in and blocked the CFC@500A nanopores. Powder X-ray Diffraction measurement (PXRD) was employed to confirm the infiltration of NaAlH<sub>4</sub>. As shown in Figure 2f, a broad peak at around 20 degree was attributed to the porous carbon framework and maintained for both CFC/NaAlH<sub>4</sub> and CFC@NaAlH<sub>4</sub>. Some impurities such as NaCl and aluminum oxide were also detected at 31, 38 degrees due to high reactivity of NaAlH<sub>4</sub> and aluminum oxidation. The typical crystalline NaAlH<sub>4</sub> peaks were not detected in CFC@NaAlH<sub>4</sub> whereas the physical mixture, CFC/NaAlH<sub>4</sub>, showed crystalline NaAlH<sub>4</sub> XRD peaks. It suggests that NaAlH<sub>4</sub> is successfully incorporated into nano-sized pores of the CFC@500A during the wet infiltration, in which case it exists as nano-crystallites or an amorphous form.<sup>[23]</sup> The

existence of intact NaAlH<sub>4</sub> was further identified by the FT-IR spectrum (Figure S28). Although the original CFC@500A peaks were coincided, AlH<sub>4</sub><sup>-</sup> stretching and bending peaks at 880 and 1670 cm<sup>-1</sup> were shown in CFC@NaAlH<sub>4</sub>, meaning that NaAlH<sub>4</sub> was incorporated and undamaged after the infiltration process. Therefore, it can be deduced that NaAlH<sub>4</sub> particles were successfully nanoconfined within the pore of CFC@500A.

To examine the dehydrogenation kinetics of CFC@NaAlH<sub>4</sub>, Temperature Programmed Desorption–Mass Spectroscopy (TPD-MS) was implemented under Ar atmosphere at 1 bar. It is known that hydrogen is released from bulk NaAlH<sub>4</sub> in a stepwise procedure (Figure 3a). In their bulk form without nanoscaling and confinement into carbon scaffolds, the kinetic barrier for dehydrogenation is significantly high, beyond the bounds of practical application. To evaluate the effect of the mesoporous carbon scaffolds, the dehydrogenation kinetics of CFC@NaAlH<sub>4</sub> was investigated while varying the heating rate as 5, 10, 15, and 20 °C/min (Figure 3b). At 5 °C/min heating rate, CFC@NaAlH<sub>4</sub> starts to desorb hydrogen below 50 °C and the peak temperature is about 80 °C, reduced by 100 °C compared with bulk NaAlH<sub>4</sub>. During desorption measurement, hydrogen is also detected at higher temperatures above 300 °C, presumably not released from the confined NaAlH<sub>4</sub> based on its desorption behavior. It is speculated that oxygen in the remained THF can form Al<sub>2</sub>O<sub>3</sub> nanoclusters, leading to release hydrogen and other volatile gases by a redox reaction.<sup>[23a, 24]</sup> In contrast with the three steps of dehydrogenation in bulk NaAlH<sub>4</sub>, the two distinguishable peaks were observed for dehydrogenation of CFC@NaAlH<sub>4</sub>, as indicated in Figure 3b. To confirm the dehydrogenation mechanism shown as two isolated peaks, the PXRD patterns of CFC@NaAlH<sub>4</sub> dehydrogenated at 120 °C—in the middle of two desorption peaks—was measured (Figure S29). Such partially dehydrogenated CFC@NaAlH<sub>4</sub> showed several peaks associated with NaH, NaCl, Al<sub>2</sub>O<sub>3</sub>, and Al particles. Specifically, Al particles exist with NaH as products of the dehydrogenation process, while NaCl was formed by a reaction between NaAlH<sub>4</sub> and Cl from the calcination process. It is noticeable that NaH was uncovered in the dehydrogenated sample at 120 °C because NaH formation is not feasible during the dehydrogenation process at such a lower temperature. In contrast, bulk NaAlH<sub>4</sub> dehydrogenated at 120 °C maintained its crystalline structure as pristine NaAlH<sub>4</sub>, not forming any products like Na<sub>3</sub>AlH<sub>6</sub> and NaH. It has been reported that Na<sub>3</sub>AlH<sub>6</sub> nanoparticles are seldom formed when the particle size decreases due to high surface energy of Na<sub>3</sub>AlH<sub>6</sub>.<sup>[25]</sup> As revealed in a phase diagram and reaction map, the altered reaction pathway from two-step decomposition (Reaction I and II a) to one-step decomposition (Reaction III) with direct NaH formation was demonstrated as the NaAlH<sub>4</sub> particle size decreases (Figure S30). Thus, the formation of NaH at 120 °C for CFC@NaAlH<sub>4</sub> confirms the alteration of the thermodynamic pathway of hydrogen release for NaAlH<sub>4</sub> as a result of nanoconfinement. Accordingly, each peak in TPD-MS measurement is in agreement with one step dehydrogenation procedure, simply separated by two different sized pores: 1-2 nm and 8-10 nm.

## RESEARCH ARTICLE

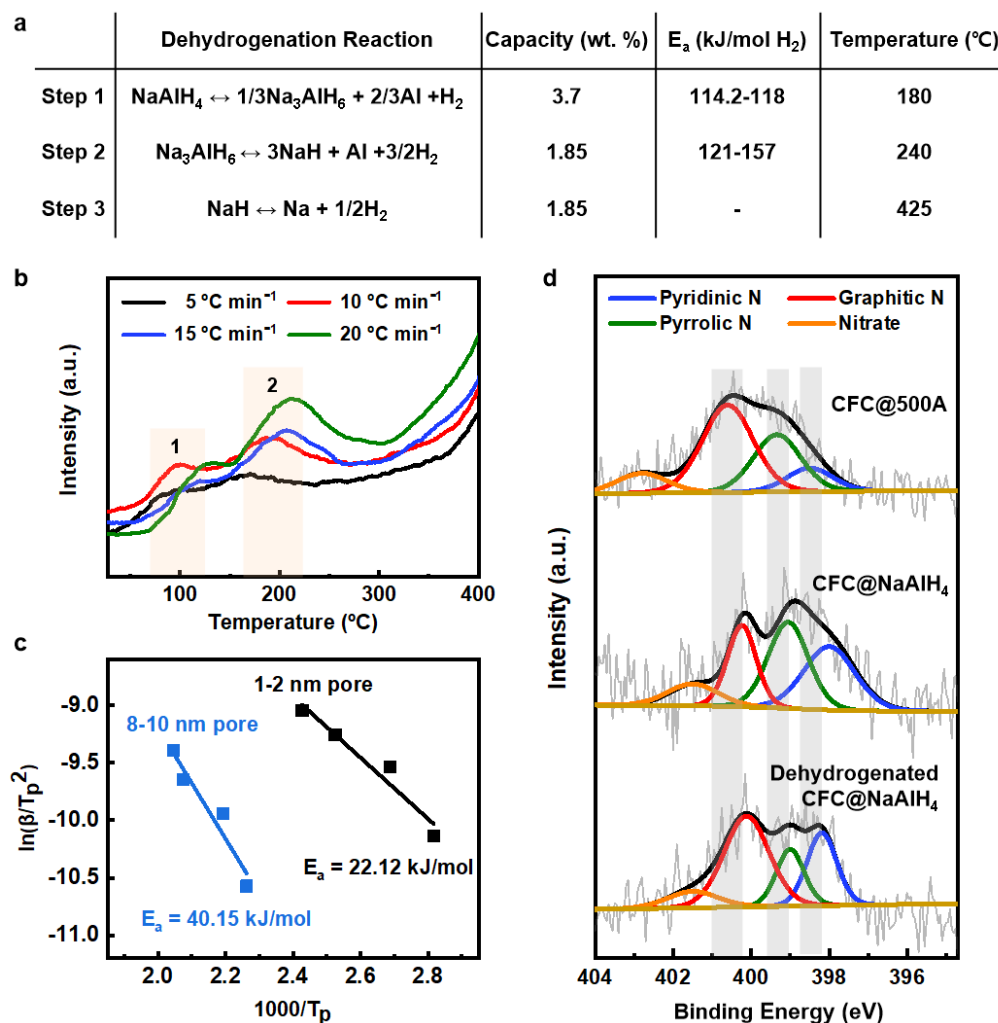


**Figure 3.** Dehydrogenation mechanism analysis of CFC@NaAlH<sub>4</sub>. a) Three steps of dehydrogenation reaction and corresponding hydrogen capacity, activation energy of dehydrogenation, and desorption temperature for bulk NaAlH<sub>4</sub>. (The activation energy of bulk NaAlH<sub>4</sub> and Na<sub>3</sub>AlH<sub>6</sub> is obtained from the literature.<sup>[26]</sup>) b) TPD-MS of desorbed hydrogen from CFC@NaAlH<sub>4</sub> while varying the heating rates (5, 10, 15, 20  $^{\circ}C/min$ ). c) Kissinger plots of CFC@NaAlH<sub>4</sub> based on TPD-MS data. d) N 1s XPS spectra of CFC@500A, CFC@NaAlH<sub>4</sub>, and dehydrogenated CFC@NaAlH<sub>4</sub>.

The activation energy of hydrogen desorption for CFC@NaAlH<sub>4</sub> was determined by the Kissinger method<sup>[27]</sup> using the peak temperatures dependent on each heating rate (Figure 3c) (the details are described in Supporting Information). The activation energies for dehydrogenation of confined NaAlH<sub>4</sub> in 1-2 nm and 8-10 nm pores were calculated as 22 kJ/mol H<sub>2</sub> and 40 kJ/mol H<sub>2</sub>, respectively. To the best of our knowledge, the CFC@NaAlH<sub>4</sub> showed the lowest dehydrogenation activation energy among other reported NaAlH<sub>4</sub>-based materials including other various transition metal catalyst doped NaAlH<sub>4</sub> (Table S3). Since some NaAlH<sub>4</sub> would react with nitrogen or oxygen contained in CFC@500A, the hydrogen capacity of infiltrated NaAlH<sub>4</sub> was approximately 3 wt. % which is lower than the theoretical value. However, with a significant reduction in the

activation energy, CFC@NaAlH<sub>4</sub> exhibited the unprecedentedly lower temperature for hydrogen release.

Such noticeable advancement in kinetics can be attributed to the synergistic effect of nanoconfinement and N-doping of CFC@500A. In general, the nanoconfinement of NaAlH<sub>4</sub> leads to the reduction in diffusion length of hydrogen, surface energy increment, and additional electronic interactions with the scaffold, which eventually contributes to the enhanced dehydrogenation kinetics or thermodynamic pathway alteration.<sup>[15a, 28]</sup> Upon nanoscaling, NaAlH<sub>4</sub> directly decomposes to NaH through the modified reaction pathway where no unstable intermediate, (Na<sub>3</sub>AlH<sub>6</sub>) is produced during dehydrogenation as opposed to the case of bulk NaAlH<sub>4</sub> (Figure 3a).<sup>[25, 29]</sup> Furthermore, it is known that nanosized NaAlH<sub>4</sub> is considerably influenced by electronegative carbon scaffolds through

## RESEARCH ARTICLE

electronic interactions.<sup>[30]</sup> Since the stability of NaAlH<sub>4</sub> is derived from ionic strength between Na<sup>+</sup> and AlH<sub>4</sub><sup>-</sup> and covalent bonding of Al-H, NaAlH<sub>4</sub> can be easily disintegrated into Na<sup>+</sup> and AlH<sub>4</sub><sup>-</sup> when the carbon scaffold provides negative charge to NaAlH<sub>4</sub>. It generates AlH<sub>3</sub> vacancy and promotes the diffusion of hydrogen through rapid transformation in hydride structure, which results in hydrogen release under mild condition. Therefore, we conclude that the nanoconfinement of NaAlH<sub>4</sub> into CFC@500A pores lowered both onset temperature and activation energy value for hydrogen desorption, ascribed by nanosizing and electronic interaction with carbon framework. Another attribute to the improved dehydrogenation kinetics of CFC@NaAlH<sub>4</sub> is the doping effect originated from an N-embedded structure of carbon scaffold. The previous studies demonstrated that the addition of nitrogen doped species into complex hydrides decreased the hydrogen release energy and facilitated the removal of hydrogen as a result of electronic charge transfer.<sup>[16c, 31]</sup> The interaction between the nitrogen in CFC@500A and the infiltrated NaAlH<sub>4</sub> was confirmed from N 1s XPS (Figure 3d). The shift toward lower binding energy suggests that the incorporated NaAlH<sub>4</sub> particles closely interact and reduce the doped nitrogen. Also, the relative intensity of graphitic nitrogen was reduced, while that of pyridinic and pyrrolic nitrogen increased after NaAlH<sub>4</sub> infiltration, indicating the increment in the relative content of Lewis base for NaAlH<sub>4</sub> (Table S4).<sup>[16c]</sup> The charge donation from nitrogen was further investigated with the dehydrogenated CFC@NaAlH<sub>4</sub>, in which case the relative content of pyridinic nitrogen decreased and its peak was shifted to higher binding energy (Figure 3d and Table S4). It suggests that the pyridinic nitrogen acts as a Lewis base to provide negative charges to Na<sup>+</sup> during hydrogen release reactions. Thus, the destabilization of NaAlH<sub>4</sub> induces the fast formation of AlH<sub>3</sub> through negative charge transfer from nitrogen to NaAlH<sub>4</sub>, resulting in NaAlH<sub>4</sub> decomposition at lower temperatures.

## Conclusion

In conclusion, we report a new and facile synthetic route for N-doped ordered mesoporous carbon structure by using microwave preferential heating and assembly, and its application as a functional scaffold for solid-state hydrogen storage materials. The rapid, selective heating of the iron oxide nanoparticles forces the nanoporous polymer to form around and wrap the nanoparticles, leading to a precursor with long range order. Upon optimizing the calcination and digestion procedures, we showed that ordered mesoporous carbons can be achieved. These ordered nanopores acted as an effective platform of NaAlH<sub>4</sub> for feasible solid-state hydrogen storage, where the synergistic effect of nanoconfinement and doped-nitrogen as a catalytic function was demonstrated. Furthermore, the lowest activation energy of NaAlH<sub>4</sub> dehydrogenation with the altered reaction pathway was presented. Together with the rapid and selective formation of the ordered porous structure through microwave heating, the nanoconfinement strategies offer tremendous potential in hydrogen storage or heterogeneous catalysis. We expect a substantial development in PHANTOM

based mesoporous material and their applications in energy and environment.

## Acknowledgements

C.T.Y. acknowledges funds provided by the King Abdullah University of Science and Technology (KAUST). E.S.C. acknowledges the support by the International Energy Joint R&D Program of the Korea Institute of Energy Technology Evaluation and Planning (KETEP), granted financial resource from the Ministry of Trade, Industry & Energy, Republic of Korea. (No. 20188520000570) and also by National R&D Program through the National Research Foundation of Korea (NRF) funded by Ministry of Science and ICT (2021R1A2C2010017).

**Keywords:** Hard template synthesis • Microwave heating • Nitrogen doped carbon • Hydrogen storage • Nanoconfinement

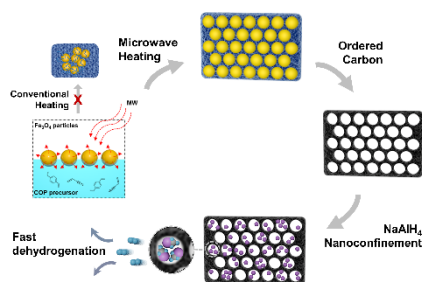
- [1] a) M. R. Benzigar, S. N. Talapaneni, S. Joseph, K. Ramadass, G. Singh, J. Scaranto, U. Ravon, K. Al-Bahily, A. Vinu, *Chem. Soc. Rev.* **2018**, *47*, 2680-2721; b) J. P. Paraknowitsch, A. Thomas, *Energy. Environ. Sci.* **2013**, *6*, 2839-2855; c) J. T. Zhang, Z. H. Xia, L. M. Dai, *Sci Adv.* **2015**, *1*; d) P. F. Zhang, J. S. Zhang, S. Dai, *Chem. Eur. J.* **2017**, *23*, 1986-1998; e) A. H. Lu, G. P. Hao, Q. Sun, *Angew. Chem. Int. Ed.* **2013**, *52*, 7930-7932; f) Z. A. Qiao, B. K. Guo, A. J. Binder, J. H. Chen, G. M. Veith, S. Dai, *Nano Lett.* **2013**, *13*, 207-212; g) S. Wang, W. C. Li, G. P. Hao, Y. Hao, Q. Sun, X. Q. Zhang, A. H. Lu, *J. Am. Chem. Soc.* **2011**, *133*, 15304-15307.
- [2] R. Ryoo, S. H. Joo, S. Jun, *J. Phys. Chem. B* **1999**, *103*, 7743-7746.
- [3] a) J. Lee, S. Han, T. Hyeon, *J. Mater. Chem.* **2004**, *14*, 478-486; b) J. Lee, S. Yoon, T. Hyeon, S. M. Oh, K. Bum Kim, *Chem. Commun.* **1999**, 2177-2178; c) R. Ryoo, S. H. Joo, M. Kruk, M. Jaroniec, *Adv. Mater.* **2001**, *13*, 677-681; d) R. Ryoo, I. S. Park, S. Jun, C. W. Lee, M. Kruk, M. Jaroniec, *J. Am. Chem. Soc.* **2001**, *123*, 1650-1657.
- [4] a) D. C. Wu, F. Xu, B. Sun, R. W. Fu, H. K. He, K. Matyjaszewski, *Chem. Rev.* **2012**, *112*, 3959-4015; b) Y. H. Deng, J. Wei, Z. K. Sun, D. Y. Zhao, *Chem. Soc. Rev.* **2013**, *42*, 4054-4070; c) S. Ghosh, N. A. Kouame, L. Ramos, S. Remita, A. Dazzi, A. Deniset-Besseau, P. Beaunier, F. Goubard, P. H. Aubert, H. Remita, *Nat. Mater.* **2015**, *14*, 505-511; d) R. Y. Zhang, Y. J. Du, D. Li, D. K. Shen, J. P. Yang, Z. P. Guo, H. K. Liu, A. A. Elzatahry, D. Y. Zhao, *Adv. Mater.* **2014**, *26*, 6749-6755; e) J. Liu, T. Y. Yang, D. W. Wang, G. Q. M. Lu, D. Y. Zhao, S. Z. Qiao, *Nat. Commun.* **2013**, *4*, 2798; f) J. Wei, D. D. Zhou, Z. K. Sun, Y. H. Deng, Y. Y. Xia, D. Y. Zhao, *Adv. Funct. Mater.* **2013**, *23*, 2322-2328.
- [5] a) X. L. Ji, K. T. Lee, R. Holden, L. Zhang, J. J. Zhang, G. A. Botton, M. Couillard, L. F. Nazar, *Nat. Chem.* **2010**, *2*, 286-293; b) H. W. Liang, W. Wei, Z. S. Wu, X. L. Feng, K. Mullen, *J. Am. Chem. Soc.* **2013**, *135*, 16002-16005; c) H. W. Liang, X. D. Zhuang, S. Bruller, X. L. Feng, K. Mullen, *Nat. Commun.* **2014**, *5*, 4973; d) T. Q. Lin, I. W. Chen, F. X. Liu, C. Y. Yang, H. Bi, F. F. Xu, F. Q. Huang, *Science* **2015**, *350*, 1508-1513; e) R. L. Liu, D. Q. Wu, X. L. Feng, K. Mullen, *Angew. Chem. Int. Ed.* **2010**, *49*, 2565-2569; f) W. H. Niu, L. G. Li, X. J. Liu, N. Wang, J. Liu, W. J. Zhou, Z. H. Tang, S. W. Chen, *J. Am. Chem. Soc.* **2015**, *137*, 5555-5562; g) X. C. Wang, K. Maeda, X. F. Chen, K. Takanahe, K. Domen, Y. D. Hou, X. Z. Fu, M. Antonietti, *J. Am. Chem. Soc.* **2009**, *131*, 1680-1681.

## RESEARCH ARTICLE

- [6] a) Z. Y. Guo, D. D. Zhou, X. L. Dong, Z. J. Qiu, Y. G. Wang, Y. Y. Xia, *Adv. Mater.* **2013**, *25*, 5668-5672; b) G. Li, J. H. Sun, W. P. Hou, S. D. Jiang, Y. Huang, J. X. Geng, *Nat. Commun.* **2016**, *7*, 10601; c) H. J. Liu, J. Wang, C. X. Wang, Y. Y. Xia, *Adv. Energy Mater.* **2011**, *1*, 1101-1108; d) M. Oschatz, L. Borchardt, K. Pinkert, S. Thieme, M. R. Lohe, C. Hoffmann, M. Benusch, F. M. Wissler, C. Ziegler, L. Giebeler, M. H. Rummeli, J. Eckert, A. Eychmüller, S. Kaskel, *Adv. Energy Mater.* **2014**, *4*, 1300645; e) L. Qie, W. M. Chen, H. H. Xu, X. Q. Xiong, Y. Jiang, F. Zou, X. L. Hu, Y. Xin, Z. L. Zhang, Y. H. Huang, *Energ. Environ. Sci.* **2013**, *6*, 2497-2504; f) Z. S. Wu, Y. Sun, Y. Z. Tan, S. B. Yang, X. L. Feng, K. Mullen, *J. Am. Chem. Soc.* **2012**, *134*, 19532-19535.
- [7] a) W. Li, F. Zhang, Y. Q. Dou, Z. X. Wu, H. J. Liu, X. F. Qian, D. Gu, Y. Y. Xia, B. Tu, D. Y. Zhao, *Adv. Energy Mater.* **2011**, *1*, 382-386; b) Z. Li, Z. W. Xu, X. H. Tan, H. L. Wang, C. M. B. Holt, T. Stephenson, B. C. Olsen, D. Mitlin, *Energ. Environ. Sci.* **2013**, *6*, 871-878; c) M. W. Schulze, L. D. McIntosh, M. A. Hillmyer, T. P. Lodge, *Nano Lett.* **2014**, *14*, 122-126.
- [8] X. W. Zhong, Y. Z. Li, L. Z. Zhang, J. Tang, X. N. Li, C. Liu, M. M. Shao, Z. G. Lu, H. Pan, B. M. Xu, *ACS Appl. Mater. Interfaces* **2019**, *11*, 2970-2977.
- [9] J. Zhou, B. Yang, Z. J. Li, L. C. Lei, X. W. Zhang, *Ind. Eng. Chem. Res.* **2015**, *54*, 2329-2338.
- [10] W. Yang, T. P. Fellinger, M. Antonietti, *J. Am. Chem. Soc.* **2011**, *133*, 206-209.
- [11] P. Zhang, L. Wang, S. Yang, J. A. Schott, X. Liu, S. M. Mahurin, C. Huang, Y. Zhang, P. F. Fulvio, M. F. Chisholm, S. Dai, *Nat. Commun.* **2017**, *8*, 15020.
- [12] C. O. Kappe, *Angew. Chem. Int. Ed.* **2004**, *43*, 6250-6284.
- [13] a) H. I. Lee, J. H. Kim, S. H. Joo, H. Chang, D. Seung, O.-S. Joo, D. J. Suh, W.-S. Ahn, C. Pak, J. M. Kim, *Carbon* **2007**, *45*, 2851-2854; b) K. S. Lakhi, W. S. Cha, J.-H. Choy, M. Al-Ejji, A. M. Abdullah, A. M. Al-Enizi, A. Vinu, *Microporous Mesoporous Mater.* **2016**, *233*, 44-52; c) U. B. Nasini, V. G. Bairi, S. K. Ramasahayam, S. E. Bourdo, T. Viswanathan, A. U. Shaikh, *J. Power Sources* **2014**, *250*, 257-265.
- [14] a) L. Schlapbach, A. Züttel, *Nature* **2001**, *414*, 353-358; b) S.-i. Orimo, Y. Nakamori, J. R. Eliseo, A. Züttel, C. M. Jensen, *Chem. Rev.* **2007**, *107*, 4111-4132.
- [15] a) C. P. Baldé, B. P. C. Hereijgers, J. H. Bitter, K. P. de Jong, *Angew. Chem. Int. Ed.* **2006**, *45*, 3501-3503; b) X. Liu, D. Peaslee, C. Z. Jost, E. H. Majzoub, *J. Phys. Chem. C* **2010**, *114*, 14036-14041; c) P. Adelhelm, P. E. de Jongh, *J. Mater. Chem.* **2011**, *21*, 2417-2427.
- [16] a) R. Xiong, G. Sang, G. Zhang, X. Yan, P. Li, Y. Yao, D. Luo, C. a. Chen, T. Tang, *Int. J. Hydrogen Energy* **2017**, *42*, 6088-6095; b) X. Zhang, Z. Ren, Y. Lu, J. Yao, M. Gao, Y. Liu, H. Pan, *ACS Appl. Mater. Interfaces* **2018**, *10*, 15767-15777; c) C. L. Carr, W. Jayawardana, H. Zou, J. L. White, F. El Gabaly, M. S. Conradi, V. Stavila, M. D. Allendorf, E. H. Majzoub, *Chem. Mater.* **2018**, *30*, 2930-2938.
- [17] C. T. Yavuz, J. T. Mayo, W. W. Yu, A. Prakash, J. C. Falkner, S. Yean, L. L. Cong, H. J. Shipley, A. Kan, M. Tomson, D. Natelson, V. L. Colvin, *Science* **2006**, *314*, 964-967.
- [18] N. A. Dogan, E. Ozdemir, C. T. Yavuz, *ChemSusChem* **2017**, *10*, 2130-2134.
- [19] a) J. C. P. Broekhoff, W. P. Vanbeek, *J. Chem Soc Farad T 1* **1979**, *75*, 42-55; b) K. S. W. Sing, D. H. Everett, R. A. W. Haul, L. Moscou, R. A. Pierotti, J. Rouquerol, T. Siemieniowska, *Pure Appl. Chem.* **1985**, *57*, 603-619; c) S. Lowell, J. E. Shields, M. A. Thomas, M. Thommes in *Characterization of porous solids and powders : surface area, pore size, and density*, Springer, Dordrecht, Boston, **2006**, pp. 347.
- [20] a) K. Saito, Y. Yamamura, Y. Miwa, S. Kutsumizu, *Phys. Chem. Chem. Phys.* **2016**, *18*, 3280-3284; b) Y. Meng, D. Gu, F. Q. Zhang, Y. F. Shi, H. F. Yang, Z. Li, C. Z. Yu, B. Tu, D. Y. Zhao, *adv. Chem. Int. Ed.* **2005**, *44*, 7053-7059.
- [21] Y. F. Zhao, X. Liu, K. X. Yao, L. Zhao, Y. Han, *Chem. Mater.* **2012**, *24*, 4725-4734.
- [22] P. J. Herley, W. Jones, *Materials Letters* **1983**, *1*, 131-136.
- [23] a) S. Chumphongphan, U. Filsø, M. Paskevicius, D. A. Sheppard, T. R. Jensen, C. E. Buckley, *Int. J. Hydrogen Energy* **2014**, *39*, 11103-11109; b) Y. Li, G. Zhou, F. Fang, X. Yu, Q. Zhang, L. Ouyang, M. Zhu, D. Sun, *Acta Mater.* **2011**, *59*, 1829-1838.
- [24] E. H. Majzoub, J. L. Herberg, R. Stumpf, S. Spangler, R. S. Maxwell, *J. Alloys. Compd.* **2005**, *394*, 265-270.
- [25] T. Mueller, G. Ceder, *ACS Nano* **2010**, *4*, 5647-5656.
- [26] a) R. K. Bhakta, S. Maharrey, V. Stavila, A. Highley, T. Alam, E. Majzoub, M. Allendorf, *Phys. Chem. Chem. Phys.* **2012**, *14*, 8160-8169; b) d. Rafi ud, Q. Xuanhui, L. Ping, L. Zhang, M. Ahmad, M. Z. Iqbal, M. Y. Rafique, M. H. Farooq, *RSC Adv.* **2012**, *2*, 4891-4903; c) G. Sandrock, K. Gross, G. Thomas, *J. Alloys. Compd.* **2002**, *339*, 299-308.
- [27] a) H. E. Kissinger, *Analytical Chemistry* **1957**, *29*, 1702-1706; b) C. P. Baldé, B. P. C. Hereijgers, J. H. Bitter, K. P. d. Jong, *J. Am. Chem. Soc.* **2008**, *130*, 6761-6765.
- [28] a) R. K. Bhakta, J. L. Herberg, B. Jacobs, A. Highley, R. Behrens, N. W. Ockwig, J. A. Greathouse, M. D. Allendorf, *J. Am. Chem. Soc.* **2009**, *131*, 13198-13199; b) X. Fan, X. Xiao, J. Shao, L. Zhang, S. Li, H. Ge, Q. Wang, L. Chen, *Nano Energy* **2013**, *2*, 995-1003; c) T. K. Nielsen, P. Javadian, M. Polanski, F. Besenbacher, J. Bystrzycki, T. R. Jensen, *J. Phys. Chem. C* **2012**, *116*, 21046-21051.
- [29] E. H. Majzoub, F. Zhou, V. Ozoliņš, *J. Phys. Chem. C* **2011**, *115*, 2636-2643.
- [30] P. A. Berseth, A. G. Harter, R. Zidan, A. Blomqvist, C. M. Araújo, R. H. Scheicher, R. Ahuja, P. Jena, *Nano Lett.* **2009**, *9*, 1501-1505.
- [31] a) L. H. Kumar, C. V. Rao, B. Viswanathan, *J. Mater. Chem. A* **2013**, *1*, 3355-3361; b) Meenakshi, D. Agnihotri, H. Sharma, *Comput. Theor. Chem.* **2016**, *1097*, 61-69; c) Y. Cho, S. Li, J. L. Snider, M. A. T. Marple, N. A. Strange, J. D. Sugar, F. El Gabaly, A. Schneemann, S. Kang, M.-h. Kang, H. Park, J. Park, L. F. Wan, H. E. Mason, M. D. Allendorf, B. C. Wood, E. S. Cho, V. Stavila, *ACS Nano* **2021**, *15*, 10163-10174.

## RESEARCH ARTICLE

## Entry for the Table of Contents



**Waves for caves.** Nitrogen doped ordered porous carbon was synthesized by microwave heating using  $\text{Fe}_3\text{O}_4$  nanoparticles as hard templates. The microwave-assisted method reduces the reaction time and provides highly ordered structure with large surface area and nitrogen doping.  $\text{NaAlH}_4$  was confined into the pores of the carbon scaffold and the hydrogen sorption kinetics is improved by the synergistic effects of nanoconfinement and nitrogen doping.

Institute and/or researcher Twitter usernames: [@caferiyavuz](#), [@KAUST\\_News](#)